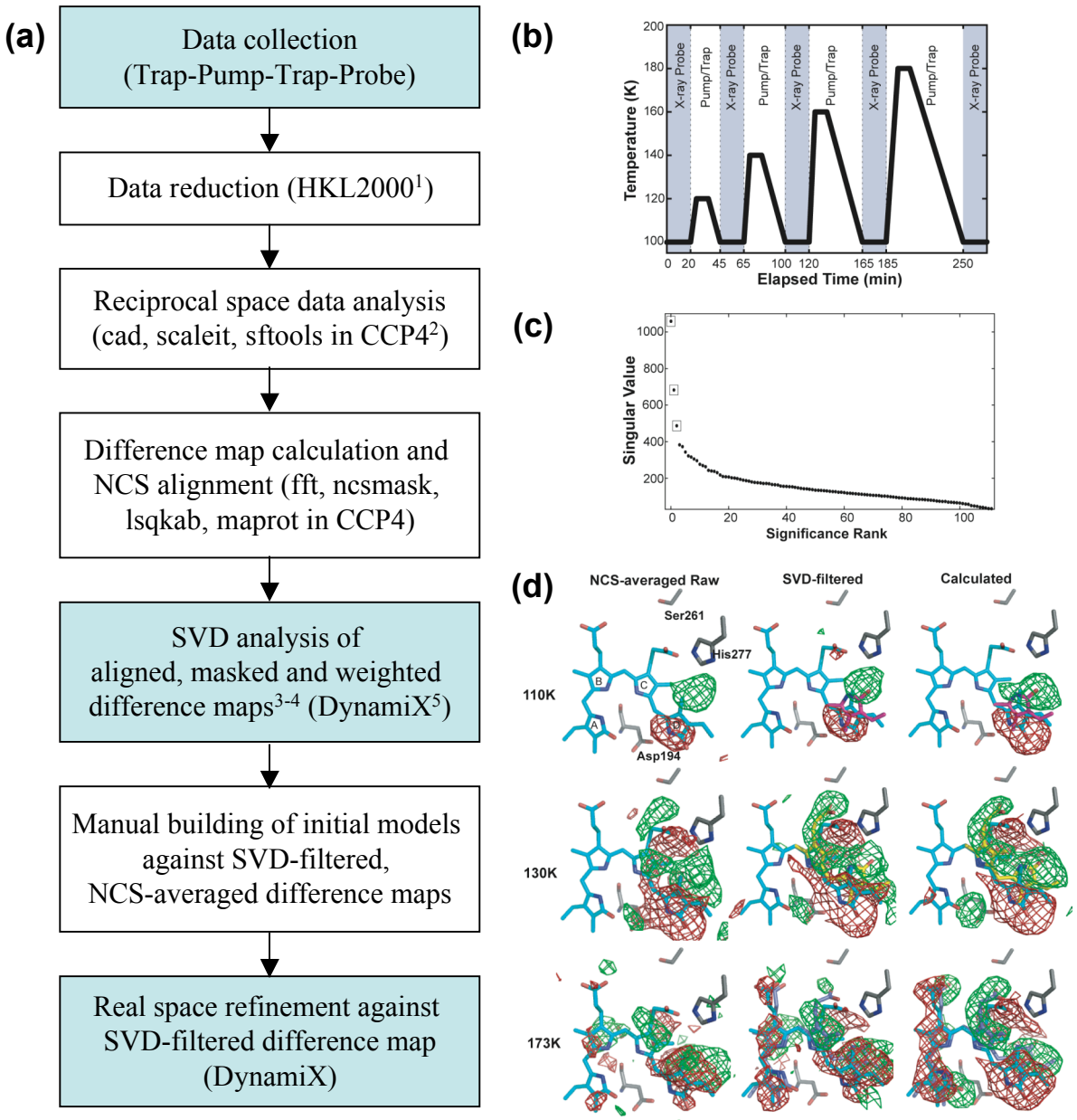

Supplementary Figure S1. (a) Flow chart of X-ray data analysis; details shown for highlighted steps in (b)-(d). (b) Scheme of Trap-Pump-Trap-Probe experiments. (c) Singular value decomposition (SVD) analysis reveals three significant singular values (marked by squares) that are used to recompose SVD-filtered difference maps (Fig. 2). (d) Side-by-side comparison shows good agreement among raw difference maps averaged over non-crystallographic symmetry (NCS) (left), SVD-filtered (middle) and calculated (right) difference maps after real space refinement at 110K, 130K and 173K. The corresponding correlation coefficients in real space between SVD-filtered and calculated maps are listed in Table S3.

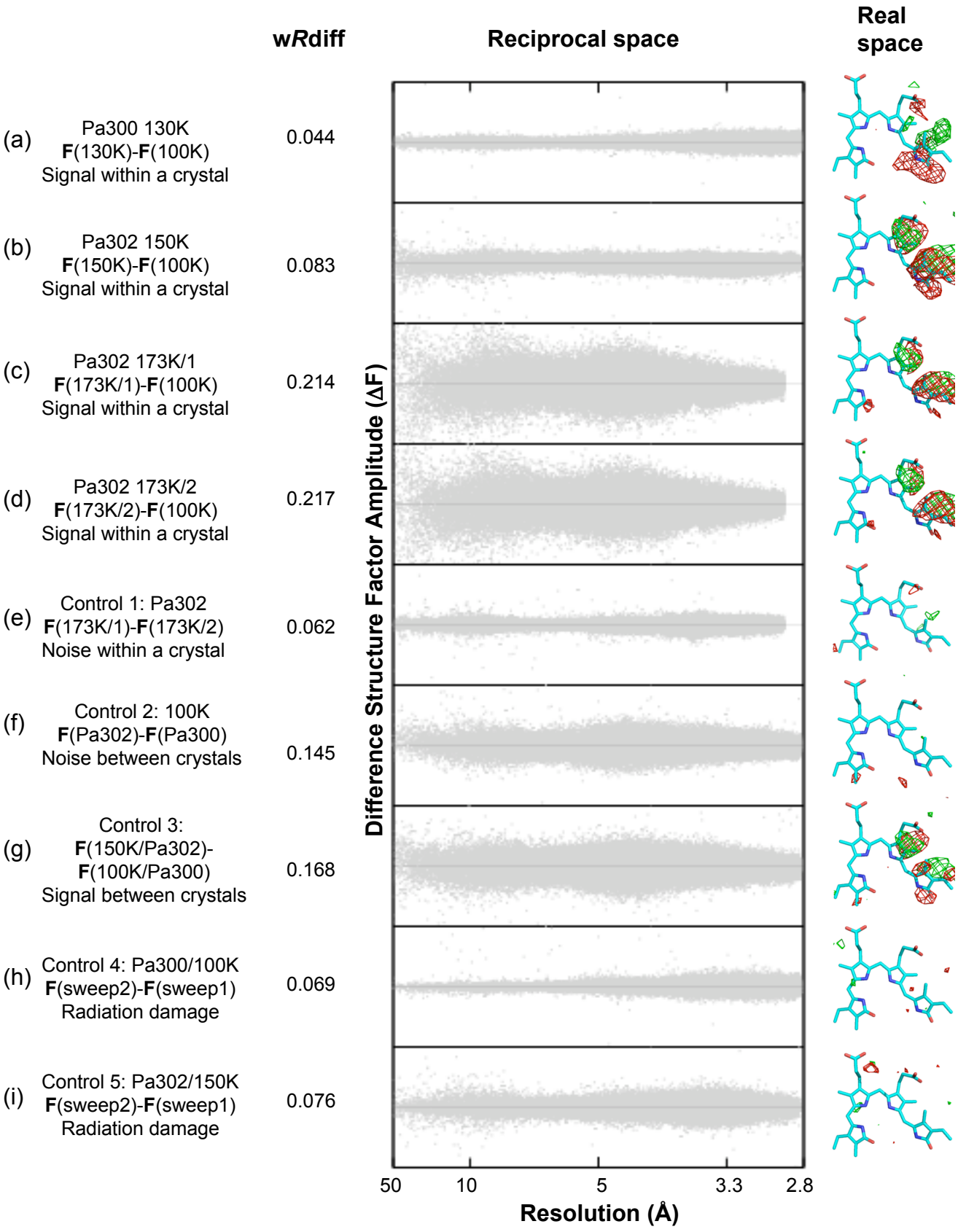
wRdiff
Reciprocal space
Real space
(a) Pa300 130K F(130K)-F(100K) Signal within a crystal
0.044
(b) Pa302 150K F(150K)-F(100K) Signal within a crystal
0.083
(c) Pa302 173K/1 F(173K/1)-F(100K) Signal within a crystal
0.214
(d) Pa302 173K/2 F(173K/2)-F(100K) Signal within a crystal
0.217
(e) Control 1: Pa302 F(173K/1)-F(173K/2) Noise within a crystal
0.062
(f) Control 2: 100K F(Pa302)-F(Pa300) Noise between crystals
0.145
(g) Control 3: F(150K/Pa302)-F(100K/Pa300) Signal between crystals
0.168
(h) Control 4: Pa300/100K F(sweep2)-F(sweep1) Radiation damage
0.069
(i) Control 5: Pa302/150K F(sweep2)-F(sweep1) Radiation damage
0.076
Difference Structure Factor Amplitude (ΔF)
50
10
5
3.3
2.8
Resolution (Å)

Supplementary Figure S2. Light-induced signals in reciprocal space and real space. Four datasets containing signal (a-d) and five control sets (e-h), all collected from two PaBphP-PCM crystals (Pa300 and Pa302; Table S1), are analyzed. The panel in the reciprocal space column shows plots of $\Delta\boldsymbol{F}$ as a function of resolution; each plot has an associated weighted difference R-factors in the column w$\boldsymbol{R}$diff (Table S1). The right panel shows corresponding raw difference electron densities (contoured at +/-4.5σ; no weighting NCS averaging or SVD filtering) in real space at the chromophore of subunit C in the asymmetric unit. A symmetrical distribution of $\Delta\boldsymbol{F}$ around 0 is usually a good indicator of proper scaling between paired structure factor amplitudes ($\Delta\boldsymbol{F}$ =0 is indicated by a horizontal gray line in each scatter plot). In the cases (a-d) where light and reference datasets are collected from the same crystal, $\boldsymbol{\Delta F}$s are relatively small at 130K (a) and 150K (b), but much larger at 173K (c and d). While small values of $\Delta\boldsymbol{F}$ are distributed across reciprocal space (a-b), strong difference signals (Δρ) with good S/N ratio are concentrated in real space near the chromophore sites (Fig. 1b). In addition, two data sets at 173K (c and d) from different segments of the same crystal display consistent signals in both real and reciprocal space (e), indicating that light-induced signals are effectively preserved at 100K without detectable decay or dark reversion during the elapsed time (hours) of data collection. Values of $\Delta\boldsymbol{F}$ in (e) also establish a baseline of random noise within the same crystal. Controls (f) and (g) examine levels of signal and noise between two different crystals. $\Delta\boldsymbol{F}$s in (f) derived from two reference data sets at 100K exhibit wider distribution than those containing a light-dependent signal at 130K(a) and 150K(b). However, larger $\Delta\boldsymbol{F}$s in reciprocal space do not result in strong signals in real space (f); $\Delta\boldsymbol{Fs}$ in this case contains both random and systematic variations from crystal to crystal. In control (g), differences between light and dark datasets from two crystals give much larger w$\boldsymbol{R}$diff, and also produce consistent, although weaker, map features comparable to (b). This positive control suggests that small, systematic difference signals rise above random noise in real space even though they appear to be completely buried in reciprocal space. This control also underlines the importance of collecting both light and reference data from the same crystal in producing difference maps of best possible S/N. Controls (h) and (i) address the effect of radiation damage. In both cases, diffraction images collected on the same crystal volume are split into two halves and merged into two separate data sets, in which the second set endures twice as much X-ray exposure as the first one. Although the overall values of $\Delta\boldsymbol{F}$ are comparable to those in (a) and (b), no significant difference densities are observed in real space, confirming that difference map features in temperature-scan data (Fig. 2) are not derived from radiation damage. We also carried out control experiments to examine the thermal effect with no additional illumination applied to the crystal at 130K. In the raw difference map ($\boldsymbol{F}_{\text{130K-dark}}$-$\boldsymbol{F}_{\text{100K-dark}}$), only weak and scattered difference densities were observed with peak levels lower than +/-3.5σ, confirming that strong difference signals shown in Fig. 1b did not arise from temperature changes.

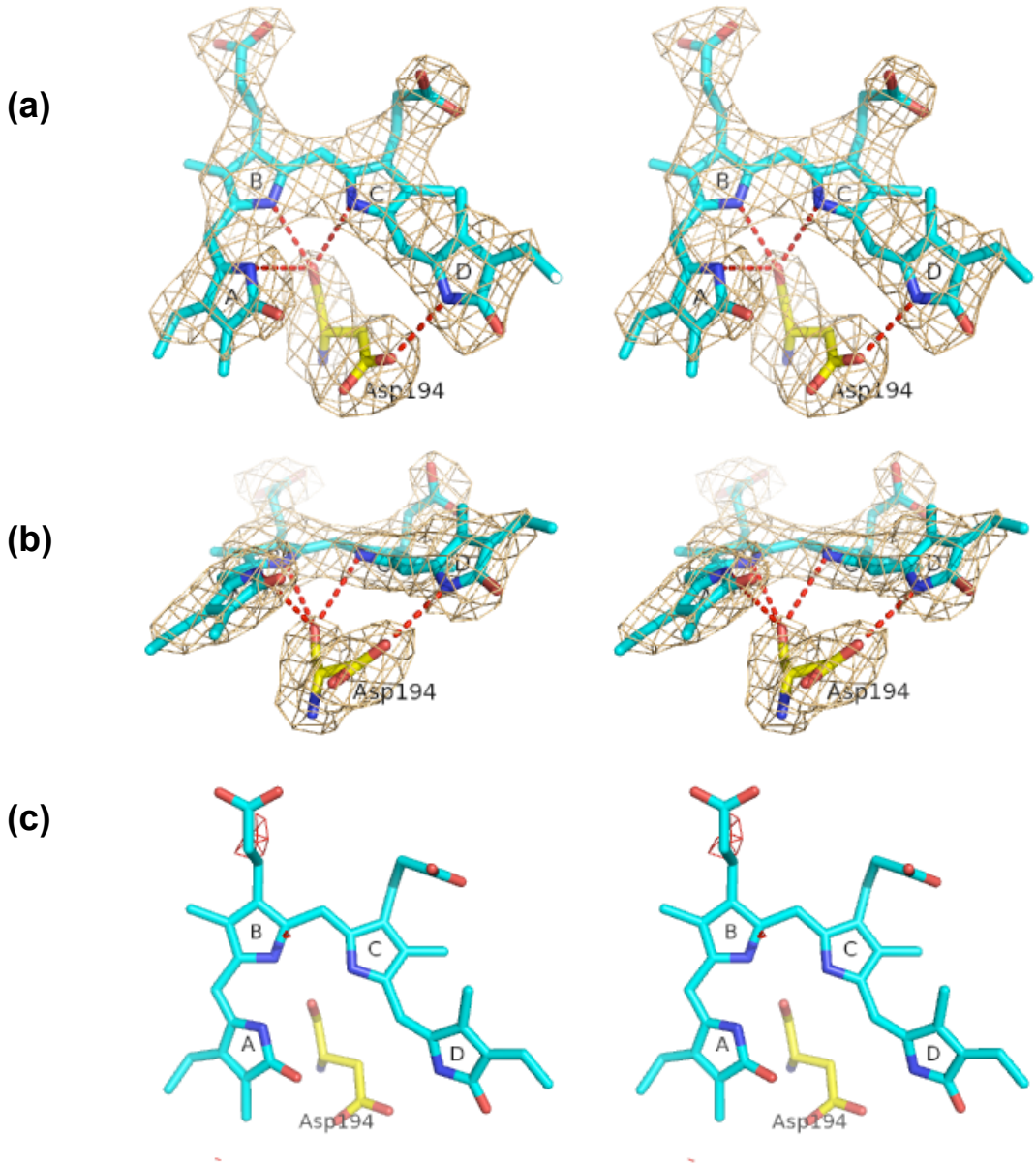

Supplementary Figure S3. Stereo views of simulated-annealing (SA) omit ***F***o-***F***c map of the biliverdin (BV) chromophore and Asp194 in the dark-adapted Pfr state of PaBphP-PCM at 2.55Å resolution (PDB ID 3NHQ). The map is contoured at 3.5σ. (a) BV adopts the *ZZE*ssa configuration in the Pfr state. A remarkable feature is the significantly "stretched" C_{15} methine bridge between rings C and D, in which the C_{14}-C_{15}-C_{16} bond angle is 141° compared with 127° in the Pr structure (PDB ID 209C)[7]. This extended BV conformation is stabilized by hydrogen bonds (red dashed lines) between pyrrole nitrogens and the main chain and side chain atoms of the highly conserved Asp194 at the β-face of BV. This accounts for high intensity of absorption at longer wavelength (λmax ~750nm) that is red-shifted compared to the Pr state (λmax ~700nm). (b). The C_{10} methine bridge between rings B and C is more twisted in the Pfr state than in the Pr structures, in which rings B and C are nearly coplanar[6-9]. (c). Refinement residual (***F***o-***F***c) map in the chromophore binding pocket contoured at +/- 3σ shows no apparent defects in our chromophore model in the Pfr state.

(a)

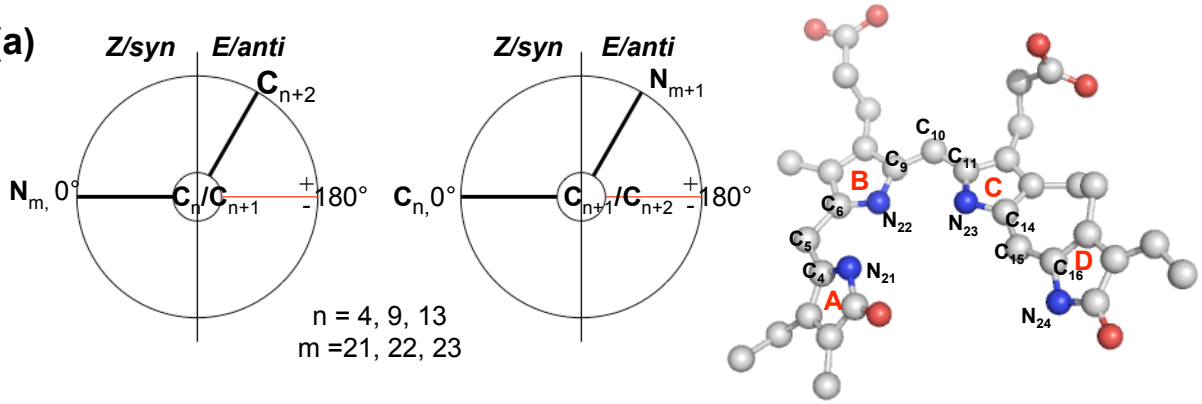

(b)

	C_5		C_{10}		C_{15}	
	N_{21}-C_4-C_5-C_6	C_4-C_5-C_6-N_{22}	N_{22}-C_9-C_{10}-C_{11}	C_9-C_{10}-C_{11}-N_{23}	N_{23}-C_{14}-C_{15}-C_{16}	C_{14}-C_{15}-C_{16}-N_{24}
Pfr	19°	8°	7°	-25°	-151°	-152°
L1	19°	8°	8°	-25°	-132°	6°
L2	24°	18°	-32°	61°	146°	-20°
L3	24°	1°	-13°	43°	128°	-25°
Pr	8°	7°	3°	-2°	-161°	36°

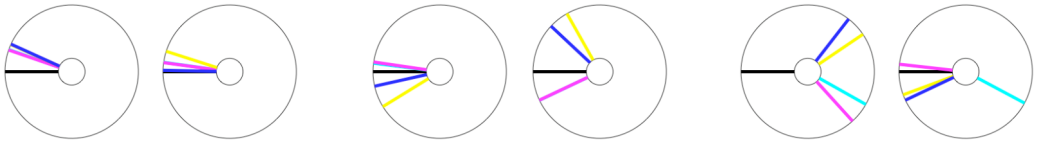

Supplementary Figure S4. Dihedral angles at the methine bridges in the parent Pfr state and three intermediate states (L1, L2 and L3). The Pr structure (PDB ID 2O9C) is included for reference[4]. (a) Diagrams (left) illustrate the configuration definitions of a linear tetrapyrrole based on the pair of dihedral angles in a methine bridge as *Z* or *E* (double bonds) and *syn* or *anti* (single bonds). Thick lines represent bonds preceding (set at 0°) and following the bond defined by the two atoms aligned at the center. Subscripts (n and m) correspond to atom numberings in the chromophore (right). (b) Dihedral angles in the C_5, C_{10} and C_{15} methine bridges in the Pfr(cyan), L1(magenta), L2(yellow) and L3(blue) structures. From Pfr to L1, *E*-to-*Z* isomerization occurs around the C_{15}-C_{16} bond. From L1 to L2, dihedral angles in the C_{15} and C_{10} methine bridges switch sign, suggesting changes in the relative arrangement between adjacent pyrrole rings. From L2 to L3, changes in dihedral angles arise from further relaxation in the C_{10} and C_5 methine bridges. Under the table, diagrams of these dihedral angles show that as the reaction proceeds from Pfr to L3, most dramatic torsional changes occur in the C_{15} methine bridge, with smaller extents in the C_{10} methine bridge, and minimal distortion in the C_5 methine bridge.

(a)

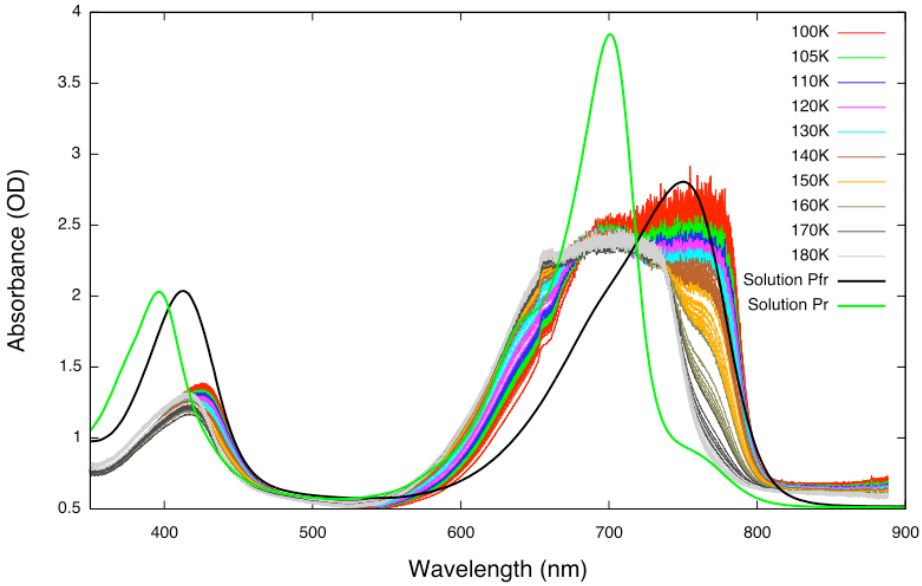
Absorbance (OD)
Wavelength (nm)
100K
105K
110K
120K
130K
140K
150K
160K
170K
180K
Solution Pfr
Solution Pr

(b)

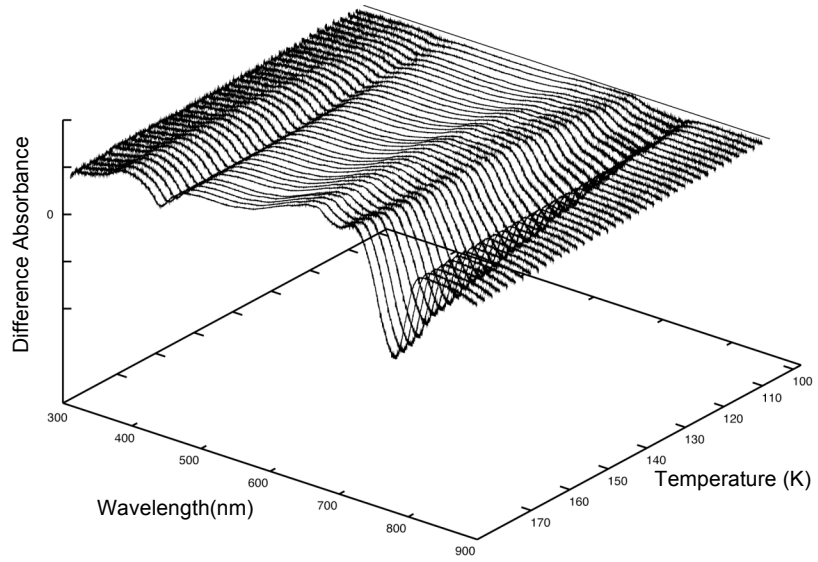
Difference Absorbance
Wavelength(nm)
Temperature (K)

(c)

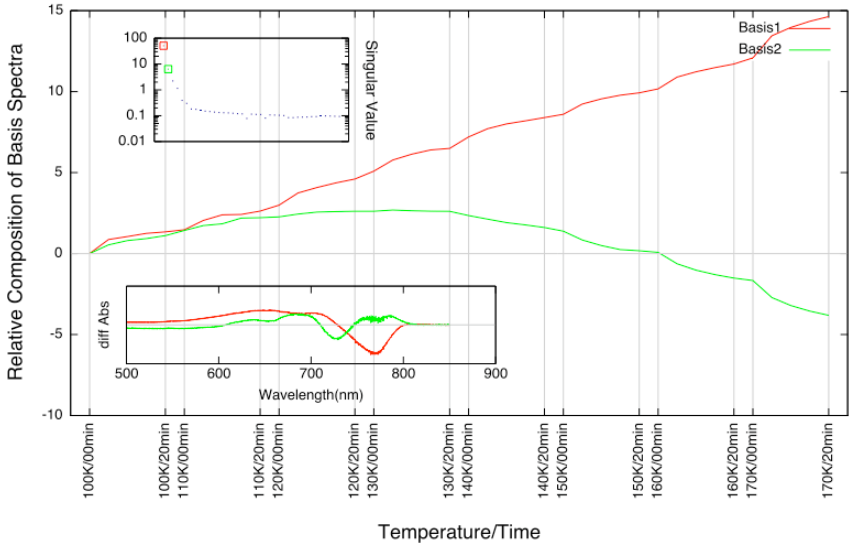
Relative Composition of Basis Spectra
Singular Value
Basis1
Basis2
diff Abs
Wavelength(nm)
Temperature/Time

Supplementary Figure S5. Microspectrophotometry of PaBphP-PCM crystals at cryogenic temperatures. (a) Dark and light-induced visible absorption spectra of a PaBphP-PCM crystal were measured at temperatures between 100K and 180K. Reference solution spectra of PaBphP-PCM at room temperature are shown in thick solid lines (black: the dark-adapted Pfr state; green: after 5min 750nm illumination). The crystal grew in the dark and was cryo-protected in dark using liquid nitrogen in mother liquor containing 20% glycerol. During four hours of data collection, the mounted crystal was illuminated under continuous unfiltered fiber optical light connected to a Xenon lamp, except in short 5-second periods during which spectra were measured. Temperature is controlled by a cryostream cooler (Oxford Cryosystems). At each pump temperature (distinguished by color), four to six spectra were taken at 5-minute intervals. Although the spectra are saturated at high OD values (>2), significant bleaching of the parent Pfr state and formation of blue-shifted species are observed. Under continuous illumination, the extent of Pfr bleaching is largely limited at temperatures below 150K. To alleviate OD saturation, a small crushed PaBphP-PCM crystal was used to collect a second temperature series. The resulting light-induced difference spectra shown in (b) were subjected to singular value decomposition analysis[10]. (c) Two basis spectra (basis 1 and 2) associated with the top two singular values (marked by red and green squares in inset) are shown, along with their compositions as a function of temperature.

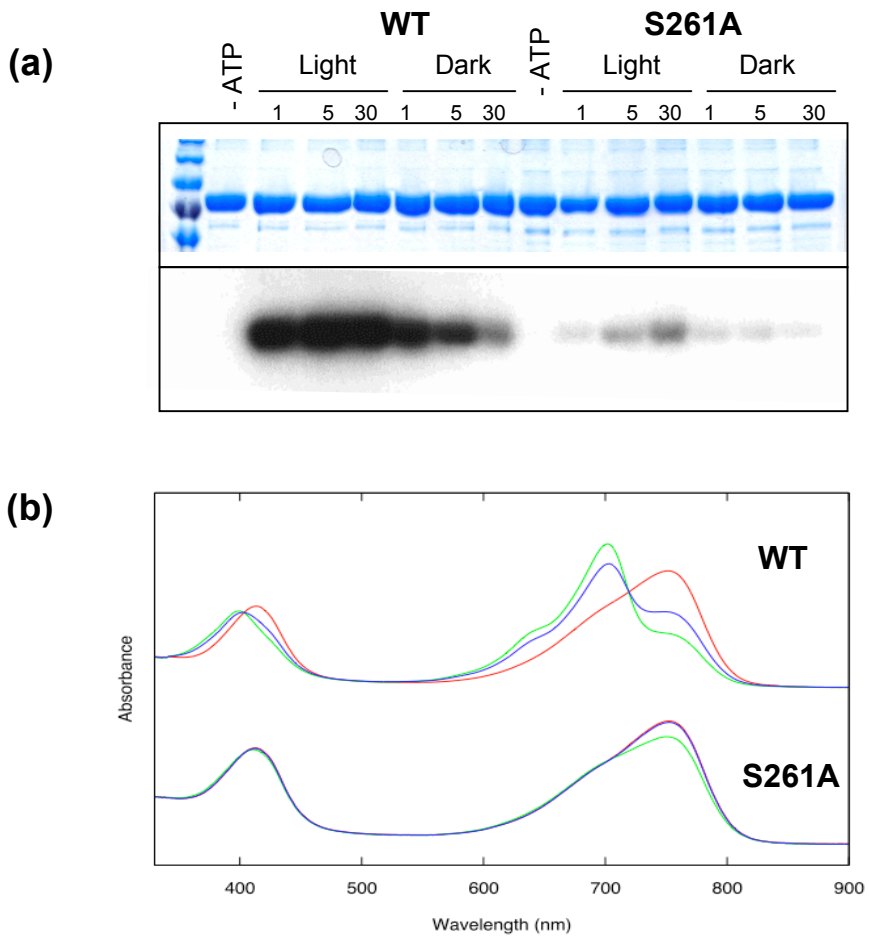

Supplementary Figure S6. *P. aeruginosa* bacteriophytochrome (PaBphP) is a light-dependent histidine kinase (HK). (a) Coomassie blue staining (top) and autoradiography (bottom) of a SDS-PAGE gel containing the same amount (3μg/lane) of wild type (WT) and point mutant S261A samples of full-length PaBphP, following the HK autophosphorylation reactions under light and dark conditions that were stopped at 1, 5 or 30 minutes after reaction initiation. In both WT and S261A, the longer the illumination, the more Pr forms and the more active the HK is. Conversely, the longer incubation in the dark, the more Pfr forms, and the less active the HK is. (b) Visible absorption spectra in solution of WT and S261A in dark (red), after 1-min illumination with unfiltered light (green), after 1-min dark reversion (blue). While the Pr state is readily detected in WT after 1-min illumination, S261A displays minimal formation of the Pr state and quickly reverts to the Pfr state[11]. S261A thus provides an easier route to achieve a homogeneous Pfr state. This dark-adapted state is otherwise hard to achieve with the WT sample at room temperature[12]. In both WT and S261A, the level of auto-phosphorylation is significantly elevated in the Pr (light) state than in the Pfr (dark) state.

Supplementary Table S1. Data collection statistics in temperature-scan experiments.

Crystals	Temp. (K)		Resolution (Å)	Completeness (%)	***R***merge*	w***R***diff† (light –dark)
Pa300	100	dark	2.7	99.9	0.086	-
	130	light	2.7	99.8	0.086	0.044
	170	light	3.3	91.4	0.136	0.198
Pa302	100	dark	2.9	99.4	0.106	-
	150	light	3.2	96.5	0.112	0.083
	173	light	3.0	99.5	0.118	0.214
	173	light	3.0	99.6	0.110	0.217
Pa305	100	dark	2.9	99.4	0.106	-
	120	light	3.1	99.8	0.132	0.054
	140	light	3.1	99.9	0.122	0.058
Pa307	100	dark	3.0	98.1	0.118	-
	100	light	3.1	97.8	0.148	0.065
	120	light	3.0	99.6	0.110	0.059
	180	light	3.8	89.5	0.112	0.191
Pa309	100	dark	3.1	91.4	0.118	-
	110	light	2.8	99.7	0.116	0.049
	160	light	3.1	90.4	0.107	0.106
Pa310	100	dark	3.1	83.9	0.147	-
	140	light	3.1	89.6	0.122	0.046
	170	light	3.2	80.1	0.118	0.151

*$\boldsymbol{R}$merge = $\sum |I - \langle I \rangle| / \sum I$, as defined in HKL2000[1].
†w$\boldsymbol{R}$diff (weighted difference R-factor) is calculated using ScaleIt of CCP4[2].
w$\boldsymbol{R}$diff = $\sum(|F_L^2 - FF_{mean}|/\sigma F_L^2 + |F_D^2 - FF_{mean}|/\sigma F_D^2) / \sum(F_L^2/\sigma F_L^2 + F_D^2/\sigma F_D^2)$, where $FF_{mean} = \sum(F_L^2/\sigma F_L^2 + F_D^2/\sigma F_D^2) / \sum(1/\sigma F_L^2 + 1/\sigma F_D^2)$, F_L is the structure factor amplitude from a light data set, and F_D is the structure factor amplitude from the dark (reference) data set at 100K.

Supplementary Table S2. Statistics of the PaBphP-PCM structure in the dark-adapted Pfr state refined using PHENIX[13].

Crystal	PaBphP-PCM in the Pfr state	
Temp (K)	100	
Overall redundancy	5.5	
Number of observed reflections	147603	
Completeness (%)	98.2 (50-3.05 Å)	82.9 (50-2.55Å)
Resolution	50-2.55Å	2.58-2.55Å (highest shell)
I/σI	23	1.8
*R*merge (I)	0.05	0.39
R-factor/*R*-free	0.215/0.258	0.346/0.396
R.m.s.d. bond (Å) /angle (°)	0.004/0.868	
Structure	Eight monomers (A, B, C, D, E, F, G, H) 4040 residues, 8 BV and 195 waters	
Space group	$C222_1$	
Cell dimension (Å)	a = 154.38; b = 162.97; c = 436.09	
PDB ID	3NHQ	

Supplementary Table S3. Real space refinement statistics of the cryo-trapped structures L1, L2 and L3.

Crystal	Pa309	Pa300	Pa302
Temp (K)	110	130	173
Target Difference map	$(\boldsymbol{F}_{\text{obs-110K}} - \boldsymbol{F}_{\text{obs-100K}})$ $\boldsymbol{\Phi}_{100K}$	$(\boldsymbol{F}_{\text{obs-130K}} - \boldsymbol{F}_{\text{obs-100K}})$ $\boldsymbol{\Phi}_{100K}$	$(\boldsymbol{F}_{\text{obs-173K}} - \boldsymbol{F}_{\text{obs-100K}})$ $\boldsymbol{\Phi}_{100K}$
Correlation coefficient ($\Delta\rho_{obs}$ vs $\Delta\rho_{calc}$)†	0.65	0.78	0.73
Relative compositions of Light Structures	L1 (0.8) L2 (0.2)	L1 (0.5) L2 (0.3) L3 (0.2)	L3 (1.0)
Residues refined	BV, His277, Ser261, Tyr163, residue 188-194, Cys12		
PDB ID	L1 (3NOP)	L2 (3NOT)	L3 (3NOU)

†$\Delta\rho_{obs}$: observed difference electron densities; $\Delta\rho_{calc}$: calculated difference electron densities based on refined structures (Pfr, L1, L2 and L3) and their relative concentrations. Correlation coefficients are calculated using difference densities within 5Å radius around the chromophore in the Pfr state.

Supplementary References

1. Otwinowski, Z. & Minor, W. Processing of X-ray Diffraction Data Collected in Oscillation Mode. Methods in Enzymology 276, 307-326 (1997).
2. Winn, M. D. et al. Overview of the CCP4 suite and current developments. Acta Crystallogr D Biol Crystallogr 67, 235-42 (2011).
3. Ren, Z. *et al*. A molecular movie at 1.8 A resolution displays the photocycle of photoactive yellow protein, a eubacterial blue-light receptor, from nanoseconds to seconds. Biochemistry 40, 13788-801 (2001).
4. Rajagopal, S., Schmidt, M., Anderson, S., Ihee, H. & Moffat, K. Analysis of experimental time-resolved crystallographic data by singular value decomposition. Acta Cryst. D60, 860-871 (2004).
5. DynamiX is a collection of software tools for analyzing dynamic crystallographic data developed by Z. Ren. Algorithms and methods are described in Ren, Z *et al*. Real space analysis of structural hetereogeneity in macromolecular crystallography. Manuscript in preparation.
6. Wagner, J. R., Brunzelle, J. S., Forest, K. T. & Vierstra, R. D. A light-sensing knot revealed by the structure of the chromophore-binding domain of phytochrome. Nature 438, 325-31 (2005).
7. Wagner, J. R., Zhang, J., Brunzelle, J. S., Vierstra, R. D. & Forest, K. T. High resolution structure of *Deinococcus* bacteriophytochrome yields new insights into phytochrome architecture and evolution. J Biol Chem 282, 12298-309 (2007).
8. Yang, X., Stojkovic, E. A., Kuk, J. & Moffat, K. Crystal structure of the chromophore binding domain of an unusual bacteriophytochrome, RpBphP3, reveals residues that modulate photoconversion. Proc Natl Acad Sci U S A 104, 12571-6 (2007).
9. Essen, L. O., Mailliet, J. & Hughes, J. The structure of a complete phytochrome sensory module in the Pr ground state. Proc Natl Acad Sci U S A 105, 14709-14 (2008).
10. Numerical Recipes in C (2nd Edition), Cambridge University Press (1992).
11. Yang, X., Kuk, J. & Moffat, K. Crystal structure of *Pseudomonas aeruginosa* bacteriophytochrome: photoconversion and signal transduction. Proc Natl Acad Sci U S A 105, 14715-20 (2008).
12. Tasler, R., Moises, T. & Frankenberg-Dinkel, N. Biochemical and spectroscopic characterization of the bacterial phytochrome of *Pseudomonas aeruginosa*. Febs J 272, 1927-36 (2005).
13. Adams, P. D. *et al*. PHENIX: building new software for automated crystallographic structure determination. Acta Crystallogr D Biol Crystallogr 58, 1948-54 (2002).